19 October 2016

Improved retrieval of land ice topography from CryoSat-2 data and its impact for volume change estimation of the Greenland Ice Sheet

Johan Nilsson[1], Alex Gardner[1], Louise Sandberg Sørensen[2] and Rene Forsberg[2]

[1]Jet Propulsion Laboratory, California University of Technology

[2] DTU Space, National Space Institute, Technical University of Denmark

Abstract

A new methodology for retrieval of glacier and ice sheet elevations and elevation changes from CryoSat-2 data is presented. Surface elevations and elevation changes determined using this approach show significant improvements over ESA's publically available Cryosat-2 elevation product (L2 Baseline-B). The results are compared to near-coincident airborne laser altimetry from NASA's Operation IceBridge and seasonal height amplitudes from the Ice, Cloud, and Elevation Satellite (ICESat).

Applying this methodology to CryoSat-2 data collected in Interferometric Synthetic Aperture mode (SIN) over the high relief regions of the Greenland ice sheet we find an improvement in the root-mean-square-error (RMSE) of 27% and 40% compared to ESA's L2 product in the derived elevation and elevation changes, respectively. In the interior part of the ice sheet, where CryoSat-2 operates in Low Resolution Mode (LRM), we find an improvement in the RMSE of 68% and 55% in the derived elevation and elevation changes, respectively. There is also an 86% improvement in the magnitude of the seasonal amplitudes when compared to amplitudes derived from ICESat data. These results indicate that the new methodology provides

improved tracking of the snow/ice surface with lower sensitivity to changes in near-surface dielectric properties.

To demonstrate the utility of the new processing methodology we produce elevations, elevation changes and total volume changes from Cryosat-2 data for the Greenland Ice Sheet during the period Jan-2011 to Jan-2015. We find that the Greenland Ice Sheet decreased in volume at rate of 289 ± 20 $km^3 a^{-1}$, with high inter-annual variability and spatial heterogeneity in rates of loss. This rate is 65 $km^3 a^{-1}$ more negative than rates determined from ESA's L2 product, highlighting the importance of Cryosat-2 processing methodologies.

1 - Introduction

The European Space Agency (ESA) launched CryoSat-2 in April 2010 tasked with monitoring the changes of the Earth's land and sea ice. CryoSat-2 carries a new type of Doppler/delay radar altimeter (Raney, 1998) referred to as SIRAL (SAR Interferometric Radar Altimeter). SIRAL operates in two different modes over land ice. Over the interior part of the ice sheets it operates as a conventional pulse limited radar system, referred to as the "Low Resolution Mode" (LRM). In more complex high-sloping terrain the system uses a novel second antenna to operate in "Interferometric Synthetic Aperture Radar" (SIN) mode. This new feature allows the satellite to monitor changes in complex terrain including ice caps, glaciers and the high relief marginal areas of the ice sheets. Such areas are sensitive to changes in climate and contribute greatly to current rates of sea level rise (e.g., Gardner et al. (2013) and Shepherd et al. (2012)).

Ku-band radar altimeters are insensitive to cloud cover providing superior coverage to laser altimeters (e.g., ICESat) but experience significant amounts of volume scattering, which is controlled by the time-evolving dielectric properties of the near-surface snow, firn, and ice (Lacroix et al., 2008; Remy et al., 2012). These effects can have large implications for the determination of mass change over a wide range of both spatial and temporal scales. Changing snow conditions can introduce time-varying biases in the data that, in combination with the radar

signals interaction with the surface, introduce large elevation biases (0.5 - 1 m) (Nilsson et al., 2015a). This, combined with other factors such as processing methodology and surface topography, makes it difficult to measure small changes for much of the word's ice covered regions (Arthern et al., 2001; Gray et al., 2015; Nilsson et al., 2015b).

The mitigation of these effects in the processing of radar altimetry data is required for improved accuracy of derived temporal and spatial changes in surface elevation of glaciers and ice sheets. Several studies have proposed different approaches to assess these effects and improve the retrieval process of surface elevation and elevation changes from radar altimetry data. These include different approaches to waveform retracking (Davis, 1993, 1997; Gray et al., 2015; Helm et al., 2014) and empirical corrections to the estimated surface elevation changes (Davis and Ferguson, 2004; Flament and Rémy, 2012; Sørensen et al., 2015; Wingham et al., 2006b; Zwally et al., 2005, 2011). Relatively little work has been done to assess methods for improving elevation and elevation changes derived from ESA's CryoSat-2 data (Abulaitijiang et al., 2015; Gray et al., 2013, 2015; Helm et al., 2014).

Here we conduct a thorough analysis of CryoSat-2 SIN and LRM waveform retracking, filtering and processing methodologies to design an optimal processing methodology for CryoSat-2 elevation retrieval over both smooth and complex ice-covered terrain. We then analyze two different approaches to determining surface elevation and volume changes from the scattered CryoSat-2 elevation retrievals. The overarching goal of this work is to develop robust and accurate elevation retrieval algorithms that are less sensitive to changes in surface and sub-surface scattering properties.

The new processing scheme is applied to estimate elevation and volume changes of the Greenland Ice Sheet for the period January 2011 to January 2015, using two independent methods to characterize the robustness of the results due to methodology. The results are compared to change estimates obtained from the ESA L2 Baseline-B surface elevation product (Bouzniac et al., 2014), high accuracy airborne data from NASA IceBridge airborne topographic

mapper and seasonal height amplitudes estimated from Ice, Cloud, and Elevation Satellite (ICESat) data.

2 - Surface elevations from CryoSat-2

2.1 - Low Resolution Mode (LRM)

The LRM mode is used over the interior parts of the ice sheet, which mostly consist of low sloping terrain. Here, SIRAL operates as a conventional pulse limited radar system with a transmission frequency of 13.6 GHz (Ku-band) and has Pulse-Limited Footprint (PLF) radius of approximately 1.5 km and a beam-limited footprint (BLF) radius of approximately 7.5 km over flat terrain (Bouzinac, 2014). The gentle terrain allows for accurate mapping of the surface elevation of the ice sheet down to decimeter-level (Brenner et al., 2007). Within the LRM waveform we define the location of the surface from the leading edge of the waveform, based on a fraction of the maximum amplitude of the received power. This approach is commonly referred to as a threshold retracker. Following Davis et al. (1997) we use 20% threshold to define the location of the surface. Davis et al. (1997) argued that a 20% threshold represents the best compromise between waveforms that are entirely dominated by either volume or surface scattering, making it suitable for obtaining estimates of surface elevation for most parts of the Greenland Ice Sheet.

The CryoSat-2 LRM radar waveforms suffer from measurement noise, in the form of speckle noise. Furthermore, over the steeper parts of the LRM-area the range gate tracking-loop can loose track of the surface, producing non-usable waveforms. To remove bad or loss of track waveforms the radar waveform (20 Hz) is first filtered using a zero-phase low pass filter to reduce speckle noise on a line-by-line basis. The signal-to-noise-ratio (SNR) of the waveform is then estimated and if the SNR < 0.5 dB the waveform is rejected. The SNR threshold was

97 empirically chosen to obtain a good trade-off between the quality of the measurements and
98 sampling.

99 Before the waveform can be retracked the first surface return (first major peak) is
100 identified within the range gate window. A copy of the waveform is heavily smoothed to remove
101 small-scale surface roughness signals, keeping the overall surface signal intact. The range gate
102 index of the first peak from the copy is then used to extract the leading edge of the original low
103 pass filtered waveform. Only leading edges with a peak index above 20 are used in the
104 retracking, as peaks before or after that can indicate troublesome surface ranging. The
105 extracted leading edge is then oversampled by a factor of 100 (c.f. (Gray et al., 2013; Helm et
106 al., 2014), and the range R between the surface and satellite is determined based on the 20%
107 threshold computed according to Davis et al. (1997). The range is then corrected for several
108 atmospheric and geophysical effects relevant to land ice studies according to Bouzinac (2014).
109 The surface elevation H of the topography, relative to the WGS84 ellipsoid, is estimated as $H =$
110 $A - R$, where A is the altitude of the satellite.

111 The measured surface return over a sloping surface does not originate from the
112 satellites nadir location, but from the “Point Of Closest Approach” (POCA) to the spacecraft
113 (Brenner et al., 1983). These off-nadir returns can introduce a large range bias to the surface,
114 depending on the magnitude of surface slope, ranging from 0-120 m (Brenner et al., 1983) as
115 the measured surface height is mapped to an erroneous position (i.e. the nadir position). To
116 mitigate the effect of this error we correct the measured range and location to the POCA point
117 using an a-prior DEM, following the approach of Bamber (1994). In contrast to previous studies
118 we account also for the local surface curvature, as Remy et al. (1989) showed that accounting
119 for surface curvature in addition to surface slope significantly improve results. The surface
120 slope, aspect and curvature are estimated from an a priori DEM. The GIMP elevation model
121 (Howat et al., 2014) was used to derive surface parameters for the slope-induced error
122 correction in the LRM mode. The DEM was resampled to 2 km resolution, using bilinear

interpolation, prior to parameter estimation, which provided the lowest root-mean-square-error and further corresponds to the pulse-limited footprint of the LRM mode.

2.2 - Interferometric Synthetic Aperture Radar Mode (SIN)

The SIN mode is used over the marginal areas of the ice sheets and other smaller glaciated areas. In these areas the SIRAL altimeter operates as a Doppler/Delay radar system (Raney, 1998). The Doppler/Delay radar allows for higher along-track resolution compared to conventional altimetry, resulting in 350 m resolution in along track and 1500 m across track. In ordinary SAR operation only the amplitude of the radar echo is measured and the phase content is discarded or ignored. With the inclusion of a second antenna on CryoSat-2, interferometric SAR can also be performed. The difference in path length between the POCA and the individual antennas introduce a phase shift between the two retrieved signals that can be related to the angle of arrival (look angle). The look angle can in turn be used to resolve the across track (across antenna) location of the echo.

Multi-look processing is applied to ESA's L1B waveform product (Bouzinac, 2014) to reduce the noise in the SIN waveform but it is still affected by speckle-noise, as is the case for the LRM waveforms. To mitigate this effect, and to help identify the leading edge of the first return, we apply speckle reduction filtering and leading edge extraction of the SIN waveforms in the same way as for the LRM processing with minor changes due to differences in range gate resolution. In this case, compared to the LRM retracking algorithm, only leading edges with a peak index in the range of 100-350 are used for retracking the radar waveform (P_w).

The estimated coherence *C* of the multi-looked waveforms is then filtered in two stages; (i) all coherence measures larger than one is set to zeros (coherence values larger than one exists in the L1B product due to unknown reasons). (ii) The coherence array, as a function of range, is filtered using a 2D 5x5 Wiener filter to remove high frequency noise. The filtering of the

147 waveform and the coherence is applied to remove noise in the recreation of the interferogram,
148 discussed below.

149 The measured differential phase ϕ of the return signal is affected by phase ambiguities;
150 a sudden shift of 2π in the measured phase. To reduce phase noise and aid the phase, an
151 unwrapping of the radar interferogram *I* is performed according to Gray et al. (2013):

152 $$I = P_w \cdot C \cdot e^{-i\phi} \quad (1)$$

153 The interferogram is then filtered using a wavelet-based de-noising technique, where the real
154 and imaginary parts of the interferogram are filtered separately. The unwrapping of the
155 interferogram allows for indirect filtering of the phase, without being affected by the phase-
156 ambiguities. Phase filtering is an important consideration as it has a direct affect on accuracy of
157 the position of the ground echo. We selected a bi-orthogonal as the mother wavelet to produce
158 the wavelet coefficients decomposed into three levels. Soft thresholding was applied to detail
159 coefficients, using a heuristic threshold rule to remove noise at every level. This was done on a
160 line-by-line basis. The final filtered differential phase was then recovered by:

161 $$\phi_f = Re\{I_f\} + Im\{I_f\} \quad (2)$$

162 To resolve the phase ambiguities the filtered phase measurements require unwrapping. The
163 phase unwrapping is done on a line-by-line basis in two directions starting from the center of
164 gravity of the waveform (Wingham et al., 1986).

165 The return power distribution of a Doppler/Delay radar system shows an important
166 distinction from those from conventional pulse-limited radar systems. Here, the point
167 corresponding to the mean surface is not located at the half-power point on the leading edge,
168 but rather closer to the maximum (Wingham et al., 2006a). Therefore a new retracker has been
169 developed, closely related to the one used in Gray et al. (2013), to allow for adaptive retracking
170 of the upper parts of the leading edge of the SAR waveform. The algorithm follows the main
171 concept of the threshold retracker, developed by Davis (1997), but instead of a pre-defined

threshold it tracks the maximum gradient of the leading edge of the oversampled waveform. We refer to this approach as that “Leading-edge Maximum Gradient retracker” (LMG).

The surface returns are geolocated using the across track look-angle θ estimated from the differential phase at the retracking point according to (Wingham et al., 2006a). This, in combination with the viewing geometry, is used to define the location of the surface return on the ground using basic across track interferometric principles. We correct θ for the interferometer surface slope error by applying the look-angle scaling factor estimated in (Galin et al., 2013).

The along-track differential phase estimate, interpolated to the retracking point, is affected by phase ambiguities not corrected for during the phase unwrapping procedure. To reduce residual phase ambiguities an a priori DEM (GIMP) is used to extract the DEM surface, resampled to 500 m resolution (corresponding roughly to the along-track sampling), elevations at the nadir and echolocation using bilinear interpolation. Over a sloping surface the surface return should always come from a position upslope from the nadir point. Therefore the following relation must hold where ($H_{echo} > H_{nadir}$) or for a more practical application ($H_{echo} - H_{nadir}) > \varepsilon$, where ε is the uncertainty of the DEM used. If this relation is violated 2π is added or subtracted to the individual along-track phase estimate, depending on the sign.

A final step is applied to correct for any lingering phase ambiguities not corrected by the a priori DEM. This step uses the assumption that the along-track phase should follow a consistent pattern over most part of the satellite ground track. Hence, any large discrepancies from the overall pattern of the along-track phase would indicate an ambiguity. The ambiguity is detected by computing the residuals of the along-track phase by removing a smoothed version of the differential phase. If any of the residuals have a magnitude larger than π it is considered ambiguous and thus corrected by adding or subtracting 2π.

3 - Surface elevation changes from CryoSat-2

3.1 – Surface fit method

The surface-fitting method is based on fitting a linear model to the elevations as a function of time and space inside a search radius of 1 km (e.g., Howat et al., 2008; Moholdt et al., 2010; Sørensen et al., 2011; Wouters et al., 2015). The linear model consists of a time-invariant (static) bi-quadratic surface model to account for variable topography inside the search radius and time-variant part used to extract the temporal change in elevation. The model consists of a total of 7-parameter whereof six of the parameters (a-coefficients) describe the bi-quadratic surface modeling function, *dh/dt* the linear elevation change rate, *t* time in decimal years, t_0 the mean time inside the footprint and ε the residuals from the linear regression.

$$h(x,y,t) = a_0 + a_1 x + a_2 y + a_3 xy + a_4 x^2 + a_5 y^2 + \frac{\partial h}{\partial t}(t - t_0) + \varepsilon \quad (3)$$

The algorithm estimates the elevation change at every echolocation (or grid-node if desired) in the data set. In each solution the signal amplitude and phase are also estimated by fitting a seasonal signal model to the surface-fit elevation residuals, according to:

$$\Delta h(t) = s_0 \cos(wt) + s_1 \sin(wt) + \varepsilon \quad (4)$$

where Δh is the elevation residuals estimated from the plan-fit model, $s_{0,1}$ are the model coefficients and t the time. The amplitude *A* is then defined as $A = \sqrt{s_0^2 + s_1^2}$ and the phase *P* as $P = \tan^{-1}\left(\frac{s_1}{s_0}\right)$.

To remove outliers an iterative 3σ-filter is used in the full model solution, i.e. the topography, trend and seasonal signal are removed, using a maximum of 5-iterations. For each iteration residuals (full-model) with an absolute value larger than 10 m are removed, as seasonal changes larger than 10 m are not expected (Moholdt et al., 2010; Qi and Braun, 2013). The data inside the 1 km cap is weighted according to their distance from the estimation point according to:

$$W = \frac{1}{\left(1+\left[\frac{d}{\rho}\right]^2\right)} \quad (5)$$

where W is the estimated weight, d the distance and ρ the correlation or resolution parameter set to 500 m. The weighting allows the solution to better reflect local signal dynamics at the prediction point.

Local elevation time-series are further computed from the elevation residuals and elevation trend from each solution, according to:

$$h(x, y, t) = (t - t_0) \cdot \frac{\partial h}{\partial t} + \varepsilon \quad (6)$$

where t is the time epochs inside the search cap, t_0 is the mean time of t, dh/dt is the estimated elevation change rate and ε is the elevation residual at each time epoch.

The elevation changes estimated from the surface-fitting method are then culled to remove outliers before spatial gridding. Elevation changes with a regression error larger than 15 m a^{-1} are removed. The resulting surface elevations are binned at 5-km resolution for outlier editing purposes. For each cell the local spatial trend is modeled as a bilinear surface, and removed. The residuals are then edited using an iterative 3σ filter until the RMS converges to 2%.

3.2 – Crossover method

The crossover method is used to derive the surface elevations at the intersection point between an ascending and descending satellite ground track separated in time (Brenner et al., 2007; Khvorostovsky, 2012; Zwally et al., 1989). The surface elevations and times are then estimated at the crossover location for each track by linear interpolation of the two closest data points for each ascending and descending track. The crossover height difference is then estimated by taking the height difference between the two tracks according to:

$$\Delta h = h_2 - h_1 + \varepsilon \quad (7)$$

were h_1 and h_2 are the surface heights at the crossover location at time epoch t_1 and t_2, respectively, and E is the random measurement error, including orbital, range and retracking errors.

This approach produces crossover height differences with scattered time-epochs ranging from 0-4 years. CryoSat-2 has a 369-day repeat orbit configuration with a 30-day sub-cycle meaning that each crossover location will be revisited every 369 days and surrounding area every 30 days. This produces annual and sub-annual crossover difference around each crossover location. This fact is used to produce elevation change rates by incorporating all multi-temporal crossover difference within a neighborhood of 2.5-km around each crossover location. The elevation change is then estimated using the same procedure described for the surface-fit method, except that a bilinear model is used to remove any spatial trends in the topography of the crossover elevations according to:

$$dh(x, y, t) = a_1 x + a_2 y + \frac{\partial h}{\partial t}(t - t_0) \quad (8)$$

where dh is the crossover height difference, t the time, t_0 is the mean reference time inside the footprint, a_1 and a_2 the across and along-track slope and dh/dt the elevation change rate. This produces elevation changes comparable in time and in spatial coverage with the surface-fit method. The same outlier editing schemes is applied to the crossover elevation change rates as for the surface-fit method.

3.3 - Gridding of sparse elevation and elevation change data

The gridding is done in a polar-stereographic projection with a latitude of origin at 70°N, central longitude of 45°W and origin at the North Pole. The projection is referenced against the WGS-84 ellipsoid and the grid-resolution. The observations derived from the surface-fit and crossover method are gridded at a resolution of 1x1-km, due to the high spatial sampling.

The method of Least Squares Collocation (LSC), described in Herzfeld (1992) is used to grid the observations onto a regular grid. LSC is similar to Kriging and allows for optimal interpolation and merging of data with different accuracies, using their inherent covariance structure. The LSC-algorithm uses the 25 closest data points in 8-quadrants surrounding the prediction point to reduce spatial biasing. The prediction equation consists of two terms where the first term is the actual prediction term and the second term accounts for the non-stationary part of the data, as described by:

$$\hat{s} = C_{sz}(C_{zz} + N)^{-1}z + \left(1 - \sum (C_{sz}(C_{zz} + N)^{-1})\right) m(z) \quad (9)$$

were $C_{\hat{s}z}$ is the cross-covariance, C_{zz} is the auto-covariance, N the diagonal noise-matrix consisting of the a priori RMS-error and $m(z)$ is the median value of the observations inside the search neighborhood.

The covariance of the data inside the local neighborhood is modeled as a function of distance away from the prediction point using a third-order Gauss-Markov model described below.

$$C(r) = C_0 \left(1 + \frac{r}{\alpha} - \frac{r^2}{2\alpha^2}\right) e^{\left(-\frac{r}{\alpha}\right)} \quad (10)$$

where r is the separation distance, C_0 the local data variance and α is a scaling factor estimated from the correlation length.

LSC interpolation provides a RMS-error for each prediction point estimated from the modeled covariance of the data according to:

$$C_{\hat{s}} = C_0 - C_{sz}(C_{zz} + N)^{-1}C_{sz}^T \quad (11)$$

where the RMSE of the prediction equals to $\sigma_{\hat{s}} = (C_{\hat{s}})^{1/2}$ and where $C_{sz}{}^T$ is the transposed cross-covariance matrix.

The elevation changes estimated from the surface-fit and crossover methods are interpolated to a regular grid using their a priori error estimated from the LSC scheme. To avoid unrealistically small errors, common in the regression errors estimated over flat terrain, a

minimum error threshold is applied. Error values smaller than a specific threshold are set to the threshold value. The threshold value is representative of the overall precision of the elevation changes over flat terrain and is set to 0.2 m a^{-1}. The data are then gridded using a 75 km correlation length determined from the comparison of CryoSat-2 elevation to airborne measurements (Section 5).

The LSC algorithm is also used to generate a DEM based on the surface elevations generated from the surface-fitting algorithm. The surface elevations generated from the surface-fit were used as input to the gridding-algorithm. The use of surface elevations from the surface-fit provides several advantages compared to the raw observations as they: provide an almost equal number of observations as the raw data, have been screened for gross outliers, have been low-pass filtered using the 1-km search radius, and are all reference to roughly the same time epoch. Further the RMSE error generated from the surface-fit estimated surface height can be used as an a priori error for the LSC gridding procedure.

The DEM is generated using the same approach as for the surface elevation changes, as described previously in the section. Before the gridding procedure is applied elevations $H < 0$ and $H > 3350$ m are removed from the data set. Further, elevations with a standard error larger than 30 m are also removed. The elevations are binned spatially into a resolution of 1000 m and inside each cell the local surface trend is removed by fitting of a planar surface, and an iterative 3σ filter is applied to the residuals to remove outliers.

4 - Surface elevations and elevation changes from ICESat

To assess basin-scale patterns of elevation change we compare elevation changes from CryoSat-2 data to elevation changes derived from Ice, Cloud, and Elevation Satellite (ICESat) data. Here we use release 33 (GLA06) data collected over the 2003-2009 period. The ICESat surface heights were used to generate surface elevation changes and seasonal parameters

according to method M3 in Sørensen et al. (2011). The derived elevation changes were corrected for the G-C offset (Borsa et al., 2014). Valid elevation retrievals were selected according to Nilsson et al. (2015b). The ICESat elevation, seasonal amplitude and phase, are then used for comparison with CryoSat-2 and to build continuous time series using the surface fit method described in Section 3.1. For the purpose of this study no correction for the inter-campaign bias was applied, as this is still an active area of investigation.

5 -Validation

Elevation and elevation change results were generated for the entire Greenland Ice Sheet using CryoSat-2 data collected between Jan-2011 and Jan-2015 using the methodology presented in (Sections 2-3) (JPL product) and by applying the methods of (Section 3) to ESA's CryoSat-2 L2 elevation products (ESA product). Surface elevations and elevation changes were validated against airborne data sets obtained from NASA's Operation Ice-Bridge Airborne Topographic Mapper (ATM), obtained from the "National Snow & Ice Data Center" (NSIDC) in the form of the ILATM2 product. The generated elevation product has a resolution of 80 m, with a 40 m spacing along-track. This mission produces both elevation and elevation changes with reported vertical accuracy of ~10 cm and temporal accuracy in the cm-level (Krabill et al., 2002).

The derived surface elevations from CryoSat-2 are differenced against ATM surface elevations within 50 m of each ATM locations. One month of CryoSat-2 data consistent in time with the ATM elevations are used for the validation to avoid biases due to temporal sampling and to obtain sufficient sample size. A total of four years of campaign data are used for the validation of the surface elevations (2011-2014). The residuals are edited using an iterative 3σ filter to remove outliers. The accuracy and precision is estimated as the mean and standard deviation of the differences, respectively. The residual distribution is further binned according to surface slope estimated from the GIMP DEM (Howat et al., 2014) resampled to 500 m. The sensitivity to surface slope (slope error) can be identified in the standard deviation of the binned

residuals and can be used to judge the quality of the produced surface elevation and elevation changes, while the binned-average for the elevations can be used to determine radar-signal penetration depth.

Surface elevation change rates estimated from three different time-periods (2012-2014, 2011-2013 and 2011-2014) of overlapping ATM observations (Krabill, 2014) are used to validate the surface elevation changes estimated from the CryoSat-2 data. The same validation methodology applied to surface elevations is applied to surface elevation changes, with a few minor modifications. First the search radius is increased to 175 m to make it conform to the ATM elevation change resolution of 250 m, as this search radius encloses the entire ATM grid cell. Secondly the estimated mean and standard deviation are multiplied with the individual time-intervals of the validation data sets to make the errors comparable, as they differ in time span.

For the surface-fit and crossover methods, near-coincident elevation change rates were compared with ATM rates (e.g., April-2011 to April-2014). This provided three validation data sets for the surface-fit method, due to its high spatial coverage. However, only the 2011-2014-validation data set could be used for the crossover method, due to the lower spatial sampling of the crossovers.

The overall accuracy and precision for both the surface elevation and elevations changes are then estimated by taking the weighted mean, using the number of observations as weights, for each data set giving an average error for each measurement mode, as seen in Table-2. The weighted average errors for each mode and method have been summarized in Table-1 and Table-2 for both the ESA's and our solutions, where the values for the individual campaigns can be found in the Supplementary material.

The estimated surface elevation changes from the two independent methods were validated separately using near-coincident ATM data. The statistics of the elevation change validation have been summarized in Table-2 for each method independently for the two modes of instrument operation. We find the lowest RMSE errors for the surface-fit method, followed by

the crossover method. This differs from the findings of Moholdt et al. (2010) who found lower intrinsic errors for the crossover method, compared to the surface-fit method when applied to ICESat data. The larger search radius used for our application of the crossover method most likely explains the difference in findings between the two studies. Further, we find that the surface-fit method provides the largest reduction in RMSE for the JPL product, corresponding to 40% and 55% for the SIN and LRM-mode, respectively.

The correlation length used to derive the number of un-correlated grid-cells, which is used to estimate the standard error, was determined from a semi-variogram analysis of the elevation change residuals from CryoSat-2 minus ATM using the data from the surface-fit method. The comparison was done for each mode separately for all the individual campaigns and multiplied with the their individual time span. The semi-variogram was then computed from all the time-invariant residuals, to maximize the spatial coverage, for each mode. Analysis of the semi-variogram showed approximate correlation lengths of 100 and 75 km for the SIN and LRM-mode respectively. These correlation lengths are inside the range of the ones found by Sørensen et al. (2011) for their analysis of ICESat data, which was found to be between 50-150 km.

The main goal of this study is not to derive or compare different types of DEM's. However, to gain insight into the overall quality of our CryoSat-2 derived DEM (referred to as JPL) we compare it to three other DEM's derived from other data sets Firstly, we compare it to a DEM derived from ESA CryoSat-2 L2 data (referred to as ESA) gridded in the same manner as our DEM (Section 3.3). Secondly we compare it to a DEM from Helm et al. (2014), also based on CryoSat-2 data from 2011-2014 (referred to as AWI). Thirdly, we compare to a DEM from Howat et al. (2014) (which was used to derive topographical parameters and corrections for the JPL CryoSat-2 data), based on photogrammetry and altimetry data from the mid 1990's to 2010 (depending on data source) co-registered to ICESat elevation data from 2003-2009 (referred to as GIMP).

These data sets were then compared to IceBridge ATM elevations, spanning the four different campaigns previously used for validation of the CryoSat-2 elevations. The DEM elevation was estimated at each ATM location, using bilinear interpolation, and the elevation difference computed as (DEM-ATM). No attempt was made to account for differences in DEM and ATM epochs. The estimation of the errors of the DEM was determined in the same way as for the individual CryoSat-2 surface heights. The results of the comparison have been summarized in Table-3, as the weighted average of the different campaigns. The values from each individual campaign can be found in the supplementary material.

Analyzing the overall RMSE we find that the AWI produces the lowest RMSE, followed by JPL, ESA and GIMP, due to AWI's lower standard deviation. However, the best accuracy is obtained by the JPL DEM, which shows the lowest elevation bias of all DEM's. The ESA derived DEM shows a slightly better standard deviation than the JPL DEM, which can be explained by higher data density in the marginal areas for the ESA data. The difference in density is due to the SNR rejection criterion applied in our elevation processing. The lower standard deviation in the AWI product is mostly likely due the use of lower resolution topography in many of the high relief areas in the 1 km elevation model, producing a smoother estimate of the surface. The GIMP data set showed higher degrees of impulse noise than the other products, explaining the higher observed standard deviation. This impulse noise is attributed to that local elevation change rate, which was not accounted for in the creation of the DEM (Howat et al., 2014). Overall we find that the JPL DEM provides a suitable compromise between resolving of local detail and the minimization of bias. Further, modification to the SNR filtering criteria will likely lead to additional improvements in the DEM.

To determine the effect of retracking on the accuracy and precision of the measured surface heights from CryoSat-2 several tests was performed over different parts of Greenland for both modes. Following the approach of Davis (1997) the accuracy (mean) and precision (standard deviation) was computed as a function of leading edge threshold (in percent). This

computation was performed using a standard leading-edge threshold retracker, referred from now on as LTH, for both the LRM and SIN mode independently. The validation was performed in the same manner as described in Section 5, where ATM elevations from 2013 was used as the surface reference.

For the LRM mode data from April 2013 from the northern parts of Greenland, spanning the region 75-81°N and 54-44°W around the North Greenland Eemian Ice Drilling camp (NEEM), was used to calculate height residuals for the different thresholds. This produced approximately 1000 comparison locations, which was used to calculate statistics. The same procedure was performed over Jakobshavn Isbræ, using the same time span, to calculate statistics for the SIN-mode providing roughly 2500 comparison locations.

The results of this analysis, summarized in Figure-2, show that for the LRM-mode the precision (as a function of threshold) follows the same behavior as observed by Davis (1997), with a decrease of precision following increasing retracking threshold. However, the most notable finding was the observed inverse relationship in precision for the SIN-mode compared to LRM. For LTH-algorithm, in the SIN-mode, we observe a clear increase in precision as the retracking threshold increases, seen in Figure-2, stabilizing around 30-40%.

Analyzing the accuracy derived from the different thresholds a clear difference in apparent penetration depth of the radar signal can be observed for the two modes. For the SIN-mode, below 40%, a positive bias is observed indicating that retracker produces elevations larger than the corresponding airborne measured heights. For thresholds larger than 40% surface penetration of the signal is observed which are in general closer to the surface compared to the LRM-mode. We attribute this to differences in the near-surface density structure covered by the two modes.

In general we conclude that for the LRM-mode applying low retracking thresholds (0-30%) reduces the magnitude of the apparent surface penetration bias and provides higher precision compared to higher thresholds. Therefore, a threshold of ~20% of the leading edge is

443 suggested for retracking surface elevations for the LRM-mode, which was also previously
444 suggested by Davis (1997) and Helm et al. (2014). However, for the SIN mode a threshold
445 below 40% is not recommended, as this produces a clear positive elevation bias and poor
446 precision, as seen in Figure-2. Analyzing the difference between the LTH and the adaptive LMG
447 algorithm, used in the SIN-mode, we find that the LMG algorithm produces superior results in
448 precision compared to the standard LTH-algorithm. Comparing the adaptive solution from LMG
449 to the optimum threshold found by the LTH-algorithm, we find a comparable magnitude of the
450 elevation bias and a 32% improvement in precision, with an overall 27% reduction in RMSE,
451 using the LMG-retracker. From this comparison between the two-retracker algorithms we
452 recommend the use of the adaptive threshold approach (LMG), as it produces an elevation
453 repeatability that exceeds that of the standard threshold retracker (LTH) and provides a low
454 penetration bias.

455 A case study was also performed to determine the different processing steps effects on
456 the quality of the retrieved elevations. For this purpose the Barnes ice cap, on Baffin Island in
457 the Canadian Arctic, was chosen due to its small size, excellent validation coverage and due to
458 that it consist mostly of super-imposed ice (reducing radar signal penetration). The ice cap saw
459 a major IceBridge ATM campaign in 2011 providing a large number of flight tracks (spanning in
460 both North-South and East-West directions) suitable for validating CryoSat-2 data. The result of
461 this case study, which is detailed in supplementary material (i.e. Table-S1) shows that the
462 filtering of the differential phase has the highest impact on the overall accuracy of the
463 observation, reducing the RMSE by 12%, followed by the ambiguity correction. This shows the
464 importance of these steps, as they can have important implications for the overall quality of the
465 retrieved elevations. This is especially true in high relief areas where small changes in the look
466 angle, or an introduced phase ambiguity, can produce large elevation errors ranging from 0-100
467 m in elevation (Brenner et al., 1983).
468

6 - Error analysis

To compute volume change errors for the two methods we divide the error budget into two main components (1) the observational standard error (ε_{obs}) and the interpolation standard error (ε_{int}). The observational error budget is estimated using the root-mean-square error (RMSE) of the difference between CryoSat-2 and airborne elevation change differences, as described in Section 5. The RMSE is estimated separately from the two different modes, with the total volume change error (ε_{vol}) being computed as the RSS of the standard elevation change error of the two modes and their corresponding area, according to:

$$\varepsilon_{vol} = \sqrt{(\varepsilon_{lrm}\, A_{lrm})^2 + (\varepsilon_{sin}\, A_{sin})^2} \quad (12)$$

were A_{lrm} and A_{sin} are the areas covered by each mode. The ε_{lrm} and ε_{sin} are the standard elevation change errors of the LRM and SIN computed from the airborne validation data sets.

The observational elevation change error is estimated from the residual elevation change differences in Table-2 for the two methods. The RMSE from the LRM/SIN errors are computed using Gaussian error propagation producing an observational elevation change error (σ_{obs}). For the surface-fit and the crossover method the interpolation error is estimated as the RMS of the LSC uncertainty grid, defined as (σ_{int}). The final elevation change error is then estimated by combing the two error sources using RSS according to:

$$\varepsilon_{mode} = \varepsilon_{dh/dt} = \sqrt{(\varepsilon_{obs})^2 + (\varepsilon_{int})^2} = \sqrt{\left(\frac{\sigma_{obs}}{\sqrt{N}}\right)^2 + \left(\frac{\sigma_{int}}{\sqrt{N}}\right)^2} \quad (13)$$

Here, N is the number of uncorrelated grid-cells estimated from empirical semi-variogram analysis of the CryoSat-2 and airborne elevation change differences, and estimated according to:

$$N = \frac{A_{mode}}{\rho_{mode}^2} \quad (14)$$

were A_{mode} is the total area of the Greenland Ice sheet (~1.7x10^6 km^2) and the correlation length ρ_{mode} of 75 and 100 km for the LRM and SIN mode respectively.

7 – Results

7.1 – Surface elevations compared to ATM

The measured surface elevations from the two CryoSat-2 products (JPL vs. ESA) showed large differences in both accuracy and precision of the elevation measurements, as seen in Table-1. The average accuracy and precision for the LRM-mode from the two products showed values of 0.00 ± 0.43 m and -1.06 ± 0.89 m for the JPL and ESA products respectively. This corresponds to an average reduction in RMSE of 68% for the JPL product compared to the ESA LRM L2 data. Further, our product shows a lower residual slope error (seen in Figure-1c below ~0.5°) indicating a lower sensitivity to the degradation of performance as the surface slope increases.

Surface elevations generated from the SIN-mode showed the same type of improvement as for the LRM-mode. Here, an average accuracy and precision was found to be -0.52 ± 0.58 m and -0.90 ± 1.05 m for the JPL and ESA SIN elevation products respectively. This further corresponds to a reduction in the average RMSE of 27% for the JPL product compared to the ESA product. For the SIN-mode the JPL processing produces a slightly lower residual slope error, compared to the ESA processor (seen in Figure-1c above ~0.5°)

Larger improvements can be observed if separating the RMSE into its mean and standard deviation, corresponding to the accuracy and precision of the measurements. Using these definitions the analysis found that there is a 45% and 52% increase in precision for the SIN and LRM mode respectively, compared to the ESA L2 product, and a 42% and 99% improvement in accuracy for the respective modes.

The implementation of the LMG SIN retracking algorithm was found to reduce noise in the retrieved surface elevations compared to conventional threshold retracking. Though roughly comparable in accuracy, the LMG shows overall higher precision over all comparable leading

edge thresholds. The adaptive nature of the algorithm provides improved estimates of surface elevation and a good trade-off between accuracy and precision.

The 20% threshold retracker implemented in the LRM-mode was also found to provide improved estimates of surface elevation (both in accuracy and precision) compared to the model-based ESA-L2 retracker. Further, it also showed lower sensitivity to the 2012 melt event, due to the lower threshold used on the leading edge of the waveform.

7.2 – Surface elevation changes compared to ATM

The estimated surface elevation changes generated from the surface-fit method also showed improvement in the estimated accuracy and precision, as seen in Table-2. Here, an overall improvement in RMSE of 55% and 40% in the LRM and SIN mode, respectively, was found when comparing against ESA L2 generated elevation changes from the same method. The average accuracy and precision, compared to ATM generated elevation changes, was found to be 0.11 ± 0.67 m (LRM) and 0.30 ± 0.58 m (SIN) for the JPL derived changes. This compared to 0.25 ± 1.51 m (LRM) and 0.34 ± 1.06 m (SIN) for the ESA derived changes. This corresponds to an increase in elevation change accuracy of 56% and 12% for the LRM and SIN-mode, respectively, for the JPL product compared to ESA L2 elevation changes. The estimated elevation changes also show an increase in precisions for the JPL product of 56% and 45% for the LRM and SIN-mode, respectively, compared to its ESA counterpart.

The estimated elevation changes of the Greenland Ice Sheet, excluding the peripheral glaciers, over the period January 2011 to January 2015 show significant differences between products (JPL and ESA) in both spatial patterns and the total magnitude (Figures 3 & 4). The estimated volume change rate from the surface-fit method is -289 ± 20 $km^3 a^{-1}$ for the JPL-product and -224 ± 38 $km^3 a^{-1}$ for the ESA-product with a mean difference of 65 $km^3 a^{-1}$. The surface-fit and crossover-method produced on the order of ~20 million and ~2.5 million usable elevation changes, respectively, providing high spatial sampling. Due to the constraint put into

541 the JPL processor the ESA L2 data produced slightly more surface-fit observations (~10%), as
542 more surface elevations were accepted.

543 The ESA product produces a more positive elevation change pattern, which can be
544 attributed to the 2012 melt event that introduced a large positive bias with a magnitude of ~0.5
545 m (Nilsson et al., 2015a). Larger differences in the marginal areas for the surface-fit methods
546 are also observed. The positive signal detected in the interior of the ESA surface-fit-solution can
547 also be found in the basin time series, correlating well with the timing of the summer of 2012
548 melt event, which for example can be seen in the time series in Figure 3. These results are in
549 agreement with earlier work demonstrating the sensitivity of the ESA retracker to the changes in
550 the volume/surface scattering ratio (Nilsson et al., 2015a).

551 We used ICESat and CryoSat-2 derived surface heights to generate time series over
552 three regions in Northeast area of Greenland (Zachariæ Isstrøm, Nioghalvfjerdsfjorden and
553 Storstrømmen glaciers) for comparison purposes. These areas have in recent time shown large
554 and rapid changes, which has been noted by, e.g., Khan et al. (2014). The selected areas were
555 defined using hydrological basins derived by Lewis and Smith (2009), seen in (Figure 6), and
556 were further divided into smaller areas around the termini to highlight performance for areas of
557 rapid change. The ICESat and CryoSat-2 surface heights were then used to generate annual
558 time-series from 2003-2015 using (Equation 6) in the surface fit method. The estimated 12 year
559 time series show overall comparable elevation change rates over both time periods (2003-2009
560 and 2010-2015), especially in the terminus areas, providing confidence that CryoSat-2 can
561 actually monitor changes in these areas.

562

563

7.3 – Seasonal phase and amplitude compared to ICESat

The amplitude of the seasonal signal (Equation 4) estimated from the surface-fit (SF) method show large differences in both magnitude and spatial variability (Figure 5). For the surface-fit method a difference in amplitude of 54% is observed between the ESA and JPL products, corresponding to area-averaged amplitude of 0.17 m or the JPL product and of 0.37 m for ESA product. The comparison with ICESat derived amplitudes from 2003-2009 estimated in (Sasgen et al., 2012) using the same methodology as used here produced an area-averaged amplitude of 0.13 m, which is in good agreement with the JPL derived amplitude. This agreement is also spatially consistent, as seen in (Figure 5), indicating low sensitivity to seasonal changes in scattering regime of the upper snowpack. The observed difference in amplitude bias, taking ICESat as the true surface amplitude while acknowledging that no inter-campaign bias has been applied and further the differences in epochs, is 0.03 ± 0.13 m for the JPL product and 0.21 ± 0.27 m for the ESA product. The smallest differences are observed at high altitudes above 2000 m a.s.l., where the three data sets show almost constant amplitude of 0.1 m (ICE/JPL) and 0.2 m (ICE/ESA), providing a factor of two larger amplitude for the ESA product. Below 2000 m a.s.l., corresponding well to the equilibrium-line-altitude (ELA) of the Greenland Ice Sheet (Poinar et al., 2015), a rapid increase in amplitude is observed for all products. This is especially true for the ESA product, which increases its magnitude by a factor of two.

Analyzing the amplitude patterns on a regional drainage basin level (Figure 5c) we find good agreement between JPL CryoSat-2 and ICESat amplitude with ESA data producing consistently larger amplitudes. Regionally, the highest amplitudes can be observed in the SE of Greenland in basins (3,4,5) and are consistent with regional precipitation patterns that show high average precipitation in these areas (Bales et al., 2009; Ettema et al., 2009).

588 The seasonal phase of the peak in amplitude of the seasonal cycle is shown in (Figures 5b and
589 5c) and shows generally good agreement between the two data sets, providing the timing of the
590 maximum of the accumulation signal, before the onset of melt, to the months of June/July for
591 both JPL and ESA CryoSat-2 data sets. The ICESat derived seasonal phase shows a higher
592 dependence on elevation where the maximum of the accumulation signal is found in late May
593 below 2000 m and late July/August above 2000 m in elevation. The ICESat discrepancies from
594 the CryoSat-2 data are found in specific basins. Disagreements between the retrieved phase of
595 the peak amplitude from Cryosat-2 and ICESat data are due to differences in temporal sampling
596 as discussed in more detail in Section 8.

597 7.4 – Volume change

598 The two volume change methods produce consistent results from JPL derived elevation
599 changes, with a difference of around 1 $km^3 a^{-1}$. The spread between volume change methods is
600 larger (50 $km^3 a^{-1}$) when using ESA L2 data. The larger discrepancy can be mostly related to the
601 sensitivity of the various methods to the melt event. The surface-fit method produces the most
602 negative number (least affected by the melt event and has the lowest estimated error) and is
603 therefore taken as the most reliable estimate for both the JPL and ESA solution.
604 Comparing the estimated volume change to other studies using CryoSat-2 we find that
605 the JPL product is less negative than that estimated by Helm et al. (2014): -375 ± 24 $km^3 a^{-1}$.
606 This difference can be attributed to difference in processing methodology and to the different
607 epoch of the data used by Helm et al. (2014) of January 2011 to January 2014. Using the
608 corresponding epoch the JPL data gives a volume change estimate, based on the surface-fit
609 method, of -353 ± 26 $km^3 a^{-1}$, well within the stated uncertainty of Helm et al. (2014).
610 To examine the regional behavior of volume change estimates of the Greenland Ice
611 Sheet, gridded values from the two methods were divided into 8-drainage basins according to
612 Zwally et al. (2012). When analyzing the elevation time-series at the basin scale clear

differences can be observed in the annual and inter-annual behaviors (Figure 4). The northern and interior basins (1, 2, 7, 8) all exhibit large differences (Table 4: 0 - 30 $km^3 a^{-1}$) in the estimated volume change rates due to changes in the scattering regime resulting from the 2012 melt event. In the majority of the southern basins (4, 5, 6, 7), located in areas with higher precipitation, both products show good agreement in both trends and seasonal amplitude estimated from the surface-fit method.

8 - Discussion

The CryoSat-2 processing methodology presented here is found to produce accurate and precise measurements of ice sheet elevation and elevation change. The main improvements have been introduced in the SIN processor with the inclusion of a novel type of land ice retracker (LMG), advanced phase filtering and the inclusion of a phase ambiguity correction scheme. This processing approach decreased the RMSE in the surface height retrieval by approximately 27% (45% and 42% improvement in precision and accuracy). This improvement further propagated into the quality of the estimated elevation changes for the SIN-mode, with the same magnitude of improvement (Table-2). The described SIN-processing also generated surface elevations and elevation changes with lower sensitivity to the local surface slope, indicating a higher degree of accuracy in the geolocation and surface range estimation.

The SIN processing methodology further includes a phase filtering and phase ambiguity correction scheme. Visual inspections of a large number of tracks have shown more coherent estimation of the surface locations in the JPL product and further the implementation of the phase-ambiguity correction greatly reduced the number of track offsets. It was also noted that a relatively course DEM (~1 km) could be used to resolve phase ambiguities. The detection and correction of phase ambiguities are relatively straightforward and rely mostly on the relative accuracy of the DEM. The implementation of the phase ambiguity correction is particularly

637 important when monitoring smaller ice caps and outlet glaciers, where frequent and large track
638 offsets can bias the estimation of the underlying topography.

639 The new LRM processing methodology focused on optimal retrieval of surface
640 elevations over the interior parts of the ice sheet. Here the choice of retracking threshold has
641 proven to be the critical factor to acquire high quality surface elevations and elevation changes.
642 The choice of 20% leading edge threshold level reduced the sensitivity to changes in the
643 scattering regime for low slope, high elevation areas. The functional-based retracking algorithm
644 used in the ESA LRM processor corresponds roughly to a 50% threshold level (Wingham et al.,
645 2006a), which appears to suffer from a higher sensitivity to changes in the scattering properties
646 (volume scattering) of the near-surface firn, as the range is reference higher up (later in time) on
647 the leading edge of the waveform. This effect can be seen in Figure 2a, and that the observed
648 negative elevation bias (Table-1) for ESA-LRM (-1.0 m) fit well with the bias for the 50% LRM
649 threshold value shown in Figure 2a. This makes the algorithm more sensitive to annual and sub-
650 annual changes in snow-packs volume/surface scattering ratio, which can produce spurious
651 changes in elevation due to changes in the near surface dielectric properties. This is clearly
652 shown in patterns of ESA product derived elevation changes (Figure 3) where a large elevation
653 bias was introduced by the 2012-melt event (Nilsson et al., 2015a). The 20% threshold is less
654 sensitive to these types of changes (Table 1 & 2) and the results are in agreement with previous
655 work that has demonstrated that the 20% threshold best represents the mean surface inside the
656 footprint when exposed to a combination of surface and volume scattering (Davis, 1997).

657 Surface elevation changes, derived from multi-temporal radar altimetry observations, are
658 typically corrected for their correlation to changes in the radar waveform shape. This is to
659 reduce the effect of changes in the volume/surface scattering ratio of the ice sheets surface
660 (Davis, 2005; Flament and Rémy, 2012; Wingham et al., 2006b; Zwally et al., 2005). This
661 inherently adds to the complexity of the processing and analysis, introducing new biases and
662 error sources in the estimated parameters. For the processing approach presented here many

of these steps can be omitted or reduced, as they are an inherent part of the improved waveform retracking. There have been attempts to remove spurious step-changes in elevation resulting from sudden changes in surface scattering characteristics (caused by the 2012 melt event) apparent in the ESA Baseline-B L2 data through post-processing strategies (Nilsson et al., 2015c and McMillan et al., 2016), but such approaches spread the bias over a longer period of time making the “jumps” less noticeable in the time series by removing the step-change but introduces longer-timescale bias of equal magnitude as the scattering layer is buried by less reflective snow and low-density firn.

The result of the validation procedure shows a larger slope dependent bias in the ESA data, both in the elevation and elevation changes (Figure-1). This is especially true for the surface elevations, which can be seen in the figures of precision and accuracy (Figure 1a and 1c), where both figures show clear linear slope for the ESA surface heights. In comparison, estimated elevations from JPL-product show relatively stable statistics over the entire slope range above 0.2°. The validation of the estimated surface elevation changes, seen in (Figure 1b) and (Figure 1d), shows the effect of the 2012 melt event on the ESA derived elevation changes below 0.2°. Further, the accuracy of the ESA derived changes show a clear negative trend as function of increased surface slope. The derived precision of the surface elevation change increases dramatically above 0.5°, as more complex topography is measured.

The JPL CryoSat-2 processing methodology produces seasonal amplitudes that are in good agreement with those derived from ICESat data, further indicating the processors abilities to track real and physical changes of the ice sheets surface. The current ESA implementation produces noisier estimates of elevation change, as indicated by the larger standard deviations of the residuals in the ESA solutions for the surface-fit and crossover-method. Figure 5 further shows an amplitude bias in the ESA data compared to the corresponding ICESat reference amplitudes. The bias is constant above the Greenland ELA located around 2000 m in altitude but increases linearly as elevations decrease below this. The linear increase in amplitude

689 seems to be connected to the higher and more variable precipitation in the ablation zone where
690 changes in the variable snow cover produces changes in apparent surface height. This is less
691 prominent for the JPL SIN and LRM retrackers. The estimated seasonal phase in Figure 5c and
692 5d show that both JPL and ESA CryoSat-2 elevation products can adequately resolve the
693 seasonal maximum of the accumulation signal. Both products provide a timing of the maximum
694 to the month of July over the entire ice sheet, independent of elevation. Assessing the CryoSat-
695 2 derived maximum one does however notice a difference between CryoSat-2 and the
696 reference ICESat dataset. This constitutes roughly a ±1 month difference depending on the
697 elevation and the location. The cause of this difference can be attributed to the temporal
698 sampling of the ICESat mission. During the mission, due to degraded laser lifespan, data was
699 only collected in campaign mode during the spring and winter times corresponding to roughly
700 two months of measurements for each period. When the CryoSat-2 data was resampled to
701 coincide with the ICESat temporal sampling the same elevation and spatial pattern in the phase
702 of the maximum seasonal amplitude was observed as determined from the ICESat data. No
703 corresponding change in amplitude was observed. This was done by selecting CryoSat-2 data
704 corresponding to the same unique months available in the total ICESat record.

705 The two independent methods used to estimate the volume change of the Greenland Ice
706 Sheet produce consistent volume change estimates. This was especially true for volume
707 changes derived from the JPL elevations, with a discrepancy of less than 1 $km^3 a^{-1}$ between
708 methods. The two methods provided the same estimate of integrated volume change but the
709 use of the surface-fit is recommended as it produces higher spatial sampling compared to the
710 crossover-method and lower errors. The good agreement between the methods further
711 indicates a strong reliability in the estimated volume change rates of the Greenland Ice Sheet
712 over the four-year period. It also shows the ability of CryoSat-2 to capture both small and large-
713 scale spatial patterns in the rugged topography along the coastline and in the interior of

714 Greenland. This is especially true in the major outlet glacier systems (e.g., Zachariæ Isstrøm,
715 Nioghalvfjerdsfjorden and Storstrømmen).

716 Studying the northern parts of the Greenland Ice Sheet we find that CryoSat-2 captures
717 both intricate and complex behavior in the marginal areas of the ice sheet. This is exemplified in
718 the NE regions of Greenland (Figure 6) near Zacahariæ Isstrøm, Nioghalvfjerdsfjorden and
719 Storstrømmen, which all show complex and localized patterns of elevation change. Here,
720 Nioghalvfjerdsbrae shows very small changes in elevation during the observational time-span,
721 while Zacahariæ Isstrøm, its major neighbor shows large negative trends in elevation change.
722 The observed behavior agrees with the observations made in recent studies by Khan et al.
723 (2014) and Mouginot et al. (2015) who document rapid retreat and drawdown of the ice-front
724 position of the Zacahariæ Isstrøm beginning in 2012. Storstrømmen outlet glacier system also
725 appears to show signs of rapid thinning at low elevations near the ice-front position while a large
726 positive signal is observed roughly 100 km upstream of the terminus. This pattern has also been
727 observed by Joughin et al., (2010) and Thomas et al., (2009), using airborne altimetry and
728 surface velocity mapping. Rates of elevation change from ICESat and CryoSat-2 data show
729 good agreement in basin-scale trends (Figure 6b,c) over the 2003-2009 and 2010-2015 time
730 spans.

731 Mass loss of the Greenland Ice Sheet was estimated for comparison purposes from the Gravity
732 Recovery Climate Experiment (GRACE) satellite for the matching CryoSat-2 time period of
733 2011-2015 (Wiese et al., 2015; Watkins et al., 2015). Converting the estimated mass change to
734 volume change, assuming no changes in firn air content over the study period and an ice
735 density of 917 kg m^{-3} (assessment of changes in firn air content is out of the scope of this
736 paper), gives an ice sheet wide rate of -305 ± 38 km^3 a^{-1} (updated to Schlegel et al., 2016). This
737 estimate is corrected for volume changes from peripheral glaciers that lost volume at a rate of
738 approximately -40 ± 27 km^3 a^{-1} (Box, 2013; Fettweis et al., 2012; Noël et al., 2015). This

739 estimate of peripheral glacier change is in agreement with the estimated volume change of –41
740 ± 8 km^3 a^{-1} from Gardner et al, (2013). The volume rate derived from GRACE data agrees well
741 with our estimated rate from CryoSat-2, where both results are within the 1σ uncertainty of each
742 other and neglecting changes in firn air content over the period of study. The observed volume
743 change rates estimated from this study are within the range of previous studies, ranging from -
744 186 to -309 km^3 a^{-1} for the time period 2003-2009, summarized by Csatho et al. (2014), using
745 the same mass to volume conversion applied to the GRACE data. A more recent study by Helm
746 et al. (2014) of -375 ± 24 km^3 a^{-1} agrees within uncertainties when differences in observation
747 periods (2011 – 2014 vs. 2011 - 2015) are taken into accounted. From this comparison we find
748 that our estimate spans both the estimate of Csatho et al. (2014) and the mass loss estimated
749 from GRACE, while acknowledging the varied time spans of the different studies.

750 9 – Summary and Conclusion

751 We conclude that the use of an adaptive retracker for the SIN-mode, based on the maximum
752 gradient method, and the use of 20% threshold retracker for the LRM-mode provide improved
753 performance to the retracker currently used for the ESA L2 elevation products. It is further
754 important, especially for the SIN-mode, to apply a leading edge discriminator to identify and
755 track the leading edge of the waveform. The functional model currently employed in the ESA
756 processor has, to the author's knowledge, no such discriminator currently implemented. This is
757 important in the SIN-mode, as it often contains multiple surface returns. The single-return model
758 applied in the ESA processor will here have issues fitting a waveform containing multiple
759 surface returns resulting in retrack jitter (Helm et al., 2014).

760 Using the new CryoSat-2 processing methodology for the LRM and SIN-mode we
761 determine the volume change of the Greenland Ice Sheet to be -289 ± 20 km^3 a^{-1} during the
762 period January 2011 to January 2015. The validation against airborne ATM surface elevations
763 and elevation changes showed an average improvement in the RMSE of the measured

764 elevations of 68% and 27% for the LRM and SIN mode respectively compared to ESA Baseline-
765 B L2 products. The new methodology also provide improved elevation changes with an
766 reduction in RMSE of 55% and 40% for the LRM and SIN mode respectively, compared to their
767 ESA L2 derived counterparts.

768 The methodology also showed less sensitivity to changes in near-surface scattering
769 properties than equivalent ESA products. The new processing methodology showed little effect
770 of slope-induced errors, providing better performance in the marginal areas of the ice sheets.
771 These improvements to the CryoSat-2 processing mitigate the need for post-processing to
772 correct correlations between changes in surface elevation and changes in the waveform shape
773 (i.e. backscatter and leading edge width etc.) that can introduce biases and add to the
774 complexity of the processing and analysis.

775 The presented CryoSat-2 processing methodology provides a lower intrinsic error in the
776 measured elevation, elevation change and volume change estimates, all of which will facilitate
777 improved understanding of the geophysical process leading to changes in land ice elevation.
778 Given the release of the ESA Baseline-C, which provides improved corrections and processing
779 mainly for the L1B product, further improvements are expected in the near future.
780 The complete set of grids used in this study is available for the public from the main author (J.
781 Nilsson) upon request and are provided in geotiff format.

782 Acknowledgement

783 We are deeply thankful for the guidance of Laurence Gray and support of David Burgess. We
784 also thank Sebastian Bjerregaard Simonsen for very fruitful discussions. Further, we thank
785 Frank Paul at the University of Zurich for providing us with polygon-outlines of the Greenland Ice
786 Sheet and to the European Space Agency for providing their CryoSat-2 L1b product. We are
787 very grateful to the editor E. Berthier, the reviewer L. Schröder and an anonymous reviewer for

their thoughtful and thorough comments that greatly improve the writing and content of the manuscript. We also thank Nicole-Jeanne Schlegel and David Wiese at the Jet Propulsion Laboratory for the use of their GRACE analysis. This publication is contribution 86 of the Nordic Centre of Excellence SVALI funded by the Nordic Top-level Research Initiative. This work was supported by funding from the NASA Cryosphere program. The research was conducted at the Jet Propulsion Laboratory, California Institute of Technology under contract with NASA.

References

Abulaitijiang, A., Andersen, O. B. and Stenseng, L.: Coastal sea level from inland CryoSat-2 interferometric SAR altimetry, Geophys. Res. Lett., 42(6), 1841–1847, doi:10.1002/2015GL063131, 2015.

Arthern, R., Wingham, D. and Ridout, A.: Controls on ERS altimeter measurements over ice sheets: Footprint-scale topography, backscatter fluctuations, and the dependence of microwave penetration depth on satellite orientation, J. Geophys. Res. Atmos., 106(D24), 33471–33484, doi:10.1029/2001JD000498, 2001.

Bales, R. C., Guo, Q., Shen, D., McConnell, J. R., Du, G., Burkhart, J. F., Spikes, V. B., Hanna, E. and Cappelen, J.: Annual accumulation for Greenland updated using ice core data developed during 2000-2006 and analysis of daily coastal meteorological data, J. Geophys. Res. Atmos., 114(6), doi:10.1029/2008JD011208, 2009.

Bamber, J. L.: Ice sheet altimeter processing scheme, Int. J. Remote Sens., 15(4), 925–938, doi:10.1080/01431169408954125, 1994.

Borsa, A. A., Moholdt, G., Fricker, H. A. and Brunt, K. M.: A range correction for ICESat and its potential impact on ice-sheet mass balance studies, Cryosphere, 8(2), 345–357, doi:10.5194/tc-8-345-2014, 2014.

Bouzinac, C.: CryoSat product handbook, European Space Agency, ESA, (https://earth.esa.int/documents/10174/125272/CryoSat_Product_Handbook) (latest checked

October 2016), 2014.

Box, J. E.: Greenland Ice Sheet Mass Balance Reconstruction. Part II: Surface Mass Balance (1840–2010)*, J. Clim., 26(18), 6974–6989, doi:10.1175/JCLI-D-12-00518.1, 2013.

Brenner, A. C., Blndschadler, R. A., Thomas, R. H. and Zwally, H. J.: Slope-induced errors in radar altimetry over continental ice sheets, J. Geophys. Res., 88(C3), 1617, doi:10.1029/JC088iC03p01617, 1983.

Brenner, A. C. ., DiMarzio, J. P. . and Zwally, H. J. .: Precision and accuracy of satellite radar and laser altimeter data over the continental ice sheets, IEEE Trans. Geosci. Remote Sens., 45(2), 321–331, doi:10.1109/TGRS.2006.887172, 2007.

Csatho, B. M., Schenk, A. F., van der Veen, C. J., Babonis, G., Duncan, K., Rezvanbehbahani, S., van den Broeke, M. R., Simonsen, S. B., Nagarajan, S. and van Angelen, J. H.: Laser altimetry reveals complex pattern of Greenland Ice Sheet dynamics., Proc. Natl. Acad. Sci. U. S. A., 111(52), 18478–83, doi:10.1073/pnas.1411680112, 2014.

Davis, C. H.: Surface and volume scattering retracking algorithm for ice sheet satellite altimetry, IEEE Trans. Geosci. Remote Sens., 31(4), 811–818, doi:10.1109/36.239903, 1993.

Davis, C. H.: A robust threshold retracking algorithm for measuring ice-sheet surface elevation change from satellite radar altimeters, IEEE Trans. Geosci. Remote Sens., 35(4), 974–979, doi:10.1109/36.602540, 1997.

Davis, C. H.: Snowfall-Driven Growth in East Antarctic Ice Sheet Mitigates Recent Sea-Level Rise, Science (80-.)., 308(5730), 1898–1901, doi:10.1126/science.1110662, 2005.

Davis, C. H. and Ferguson, A. C.: Elevation change of the antarctic ice sheet, 1995-2000, from ERS-2 satellite radar altimetry, IEEE Trans. Geosci. Remote Sens., 42(11), 2437–2445, doi:10.1109/TGRS.2004.836789, 2004.

Ettema, J., Van Den Broeke, M. R., Van Meijgaard, E., Van De Berg, W. J., Bamber, J. L., Box, J. E. and Bales, R. C.: Higher surface mass balance of the Greenland ice sheet revealed by high-resolution climate modeling, Geophys. Res. Lett., 36(12), 1–5,

839 doi:10.1029/2009GL038110, 2009.
840 Fettweis, X., Franco, B., Tedesco, M., van Angelen, J. H., Lenaerts, J. T. M., van den Broeke,
841 M. R. and Gallée, H.: Estimating Greenland ice sheet surface mass balance contribution to
842 future sea level rise using the regional atmospheric climate model MAR, Cryosph., 7, 469–489,
843 doi:10.5194/tcd-6-3101-2012, 2012.
844 Flament, T. and Rémy, F.: Dynamic thinning of Antarctic glaciers from along-track repeat radar
845 altimetry, J. Glaciol., 58(211), 830–840, doi:10.3189/2012JoG11J118, 2012.
846 Galin, N., Wingham, D. J., Cullen, R., Fornari, M., Smith, W. H. F. and Abdalla, S.: Calibration of
847 the CryoSat-2 interferometer and measurement of across-track ocean slope, IEEE Trans.
848 Geosci. Remote Sens., 51(1), 57–72, doi:10.1109/TGRS.2012.2200298, 2013.
849 Gardner, A. S., Moholdt, G., Cogley, J. G., Wouters, B., Arendt, A. a, Wahr, J., Berthier, E.,
850 Hock, R., Pfeffer, W. T., Kaser, G., Ligtenberg, S. R. M., Bolch, T., Sharp, M. J., Hagen, J. O.,
851 van den Broeke, M. R. and Paul, F.: A reconciled estimate of glacier contributions to sea level
852 rise: 2003 to 2009., Science, 340(6134), 852–7, doi:10.1126/science.1234532, 2013.
853 Gray, L., Burgess, D., Copland, L., Cullen, R., Galin, N., Hawley, R. and Helm, V.:
854 Interferometric swath processing of Cryosat data for glacial ice topography, Cryosph., 7(6),
855 1857–1867, doi:10.5194/tc-7-1857-2013, 2013.
856 Gray, L., Burgess, D., Copland, L., Demuth, M. N., Dunse, T., Langley, K. and Schuler, T. V.:
857 CryoSat-2 delivers monthly and inter-annual surface elevation change for Arctic ice caps,
858 Cryosph., 9(5), 1895–1913, doi:10.5194/tc-9-1895-2015, 2015.
859 Helm, V., Humbert, A. and Miller, H.: Elevation and elevation change of Greenland and
860 Antarctica derived from CryoSat-2, Cryosph., 8(4), 1539–1559, doi:10.5194/tc-8-1539-2014,
861 2014.
862 Herzfeld, U. C.: Least-squares collocation, geophysical inverse theory and geostatistics: a bird's
863 eye view, Geophys. J. Int., 111(2), 237–249, doi:10.1111/j.1365-246X.1992.tb00573.x, 1992.
864 Howat, I. M., Smith, B. E., Joughin, I. and Scambos, T. A.: Rates of southeast Greenland ice

volume loss from combined ICESat and ASTER observations, Geophys. Res. Lett., 35(17), 1–5, doi:10.1029/2008GL034496, 2008.

Howat, I. M., Negrete, A. and Smith, B. E.: The Greenland Ice Mapping Project (GIMP) land classification and surface elevation data sets, Cryosph., 8(4), 1509–1518, doi:10.5194/tc-8-1509-2014, 2014.

Joughin, I., Smith, B. E., Howat, I. M., Scambos, T. and Moon, T.: Greenland flow variability from ice-sheet-wide velocity mapping, J. Glaciol., 56(197), 415–430, doi:10.3189/002214310792447734, 2010.

Keith Raney, R.: The delay/doppler radar altimeter, IEEE Trans. Geosci. Remote Sens., 36(5), 1578–1588, doi:10.1109/36.718861, 1998.

Khan, S. a, Kjaer, K. H., Bevis, M., Bamber, J. L., Wahr, J., Kjeldsen, K. K., Bjork, A. a, Korsgaard, N. J., Stearns, L. a, van den Broeke, M. R., Liu, L., Larsen, N. K. and Muresan, I. S.: Sustained mass loss of the northeast Greenland ice sheet triggered by regional warming, Nat. Clim. Chang., 4(4), 292–299, doi:10.1038/nclimate2161, 2014.

Khvorostovsky, K. S.: Merging and Analysis of Elevation Time Series Over Greenland Ice Sheet From Satellite Radar Altimetry, IEEE Trans. Geosci. Remote Sens., 50(1), 23–36, doi:10.1109/TGRS.2011.2160071, 2012.

Krabill, W. B., Abdalati, W., Frederick, E. B., Manizade, S. S., Martin, C. F., Sonntag, J. G., Swift, R. N., Thomas, R. H. and Yungel, J. G.: Airborne laser altimetry mapping of the Greenland ice sheet : application to mass balance assessment, J. Geodyn., 34, 357–376, doi:10.1016/s0264-3707(02)00048-0, 2002.

Lacroix, P., Dechambre, M., Legrésy, B., Blarel, F. and Rémy, F.: On the use of the dual-frequency ENVISAT altimeter to determine snowpack properties of the Antarctic ice sheet, Remote Sens. Environ., 112, 1712–1729, doi:10.1016/j.rse.2007.08.022, 2008.

Lewis, S. M. and Smith, L. C.: Hydrologic drainage of the Greenland Ice Sheet, Hydrol. Process., 23(14), 2004–2011, doi:10.1002/hyp.7343, 2009.

McMillan, M., Leeson, A., Shepherd, A., Briggs, K., Armitage, T. W. K., Hogg, A., Kuipers Munneke, P., van den Broeke, M., Noël, B., van de Berg, W. J., Ligtenberg, S., Horwath, M., Groh, A., Muir, A. and Gilbert, L.: A high-resolution record of Greenland mass balance, Geophys. Res. Lett., 43(13), 7002–7010, doi:10.1002/2016GL069666, 2016.

Moholdt, G., Nuth, C., Hagen, J. O. and Kohler, J.: Recent elevation changes of Svalbard glaciers derived from ICESat laser altimetry, Remote Sens. Environ., 114(11), 2756–2767, doi:10.1016/j.rse.2010.06.008, 2010.

Mouginot, J., Rignot, E., Scheuchl, B., Fenty, I., Khazendar, A., Morlighem, M., Buzzi, A. and Paden, J.: Fast retreat of Zachariae Isstrom, northeast Greenland, Science (80-.)., 350(6266), 1357–1361, doi:10.1126/science.aac7111, 2015.

Nilsson, J., Vallelonga, P., Simonsen, S. B., Sørensen, L. S., Forsberg, R., Dahl-Jensen, D., Hirabayashi, M., Goto-Azuma, K., Hvidberg, C. S., Kjaer, H. A. and Satow, K.: Greenland 2012 melt event effects on CryoSat-2 radar altimetry, Geophys. Res. Lett., 42(10), 3919–3926, doi:10.1002/2015GL063296, 2015a.

Nilsson, J., Sandberg Sørensen, L., Barletta, V. R. and Forsberg, R.: Mass changes in Arctic ice caps and glaciers: implications of regionalizing elevation changes, Cryosph., 9(1), 139–150, doi:10.5194/tc-9-139-2015, 2015b.

Nilsson, J, Forsberg, R and Sandberg Sørensen, L.: Cryosphere Monitoring from Satellites and Aircrafts, Ph.D. thesis, Technical University of Denmark, Kgs. Lyngby, 2015c.

Noël, B., van de Berg, W. J., van Meijgaard, E., Kuipers Munneke, P., van de Wal, R. S. W. and van den Broeke, M. R.: Evaluation of the updated regional climate model RACMO2.3: summer snowfall impact on the Greenland Ice Sheet, Cryosph., 9(5), 1831–1844, doi:10.5194/tc-9-1831-2015, 2015.

Poinar, K., Joughin, I., Das, S. B., Behn, M. D., Lenaerts, J. T. M. and van den Broeke, M. R.: Limits to future expansion of surface-melt-enhanced ice flow into the interior of western Greenland, Geophys. Res. Lett., 42(6), 1800–1807, doi:10.1002/2015GL063192, 2015.

917 Remy, F., Mazzega, P., Houry, S., Brossier, C. and Minster, J. F.: Mapping of the topography of
918 continental ice by inversion of satellite-altimeter data, J. Glaciol., 35(119), 98–107,
919 doi:10.3189/002214389793701419, 1989.
920 Remy, F., Flament, T., Blarel, F. and Benveniste, J.: Radar altimetry measurements over
921 antarctic ice sheet: A focus on antenna polarization and change in backscatter problems, Adv.
922 Sp. Res., 50(8), 998–1006, doi:10.1016/j.asr.2012.04.003, 2012.
923 Sasgen, I., van den Broeke, M., Bamber, J. L., Rignot, E., Sørensen, L. S., Wouters, B.,
924 Martinec, Z., Velicogna, I. and Simonsen, S. B.: Timing and origin of recent regional ice-mass
925 loss in Greenland, Earth Planet. Sci. Lett., 333–334, 293–303, doi:10.1016/j.epsl.2012.03.033,
926 2012.
927 N.-J. Schlegel, D.N. Wiese, E.Y. Larour, M.M. Watkins, J.E. Box, X. Fettweis, and M.R.
928 van den Broeke, Application of GRACE to the assessment of model-based estimates of
929 monthly Greenland Ice Sheet mass balance (2003–2012), The Cryosphere, 10, 1965-
930 1989, doi:10.5194/tc-10-1965-2016.
931 Shepherd, A., Ivins, E. R., A, G., Barletta, V. R., Bentley, M. J., Bettadpur, S., Briggs, K. H.,
932 Bromwich, D. H., Forsberg, R., Galin, N., Horwath, M., Jacobs, S., Joughin, I., King, M. A.,
933 Lenaerts, J. T. M., Li, J., Ligtenberg, S. R. M., Luckman, A., Luthcke, S. B., McMillan, M.,
934 Meister, R., Milne, G., Mouginot, J., Muir, A., Nicolas, J. P., Paden, J., Payne, A. J., Pritchard,
935 H., Rignot, E., Rott, H., Sorensen, L. S., Scambos, T. A., Scheuchl, B., Schrama, E. J. O.,
936 Smith, B., Sundal, A. V., van Angelen, J. H., van de Berg, W. J., van den Broeke, M. R.,
937 Vaughan, D. G., Velicogna, I., Wahr, J., Whitehouse, P. L., Wingham, D. J., Yi, D., Young, D.
938 and Zwally, H. J.: A Reconciled Estimate of Ice-Sheet Mass Balance, Science (80-.).,
939 338(6111), 1183–1189, doi:10.1126/science.1228102, 2012.
940 Sørensen, L. S., Simonsen, S. B., Nielsen, K., Lucas-Picher, P., Spada, G., Adalgeirsdottir, G.,
941 Forsberg, R. and Hvidberg, C. S.: Mass balance of the Greenland ice sheet (2003-2008) from

ICESat data - The impact of interpolation, sampling and firn density, Cryosphere, 5(1), 173–186, doi:10.5194/tc-5-173-2011, 2011.

Sørensen, L. S., Simonsen, S. B., Meister, R., Forsberg, R., Levinsen, J. F. and Flament, T.: Envisat-derived elevation changes of the Greenland ice sheet, and a comparison with ICESat results in the accumulation area, Remote Sens. Environ., 160, 56–62, doi:10.1016/j.rse.2014.12.022, 2015.

Thomas, R., Frederick, E., Krabill, W., Manizade, S. and Martin, C.: Recent changes on Greenland outlet glaciers, J. Glaciol., 55(189), 147–162, doi:10.3189/002214309788608958, 2009.

Watkins, M. M., Wiese, D. N., Yuan, D., Boening, C. and Landerer, F. W.: Improved methods for observing Earth's time variable mass distribution with GRACE using spherical cap mascons, J. Geophys. Res. Solid Earth, 120(4), 2648–2671, doi:10.1002/2014JB011547, 2015.

Wenlu Qi and Braun, A.: Accelerated elevation change of Greenland's Jakobshavn glacier observed by ICESat and IceBridge, IEEE Geosci. Remote Sens. Lett., 10(5), 1133–1137, doi:10.1109/LGRS.2012.2231954, 2013.

Wiese, D. N., Yuan, D.-N., Boening, C., Landerer, F. W., and Watkins, M. M.: JPL GRACE Mascon Ocean, Ice, and Hydrology Equivalent Water Height RL05M.1 CRI Filtered, Ver. 2, PO.DAAC, CA, USA, doi:10.5067/TEMSC-OLCR5, 2015.

Wingham, D. J., Rapley, C. G. and Griffiths, H.: New Techniques in Satellite Altimeter Tracking Systems, in Proceedings of the IGARSS Symposium, Zurich, pp. 1339–1344, ESA SP-254, Zurich., 1986.

Wingham, D. J., Francis, C. R., Baker, S., Bouzinac, C., Brockley, D., Cullen, R., de Chateau-Thierry, P., Laxon, S. W., Mallow, U., Mavrocordatos, C., Phalippou, L., Ratier, G., Rey, L., Rostan, F., Viau, P. and Wallis, D. W.: CryoSat: A mission to determine the fluctuations in Earth's land and marine ice fields, Adv. Sp. Res., 37(4), 841–871, doi:10.1016/j.asr.2005.07.027, 2006a.

968 Wingham, D. J., Shepherd, a, Muir, a and Marshall, G. J.: Mass balance of the Antarctic ice
969 sheet., Philos. Trans. A. Math. Phys. Eng. Sci., 364(1844), 1627–35,
970 doi:10.1098/rsta.2006.1792, 2006b.
971 Wouters, B., Martin-Espanol, A., Helm, V., Flament, T., van Wessem, J. M., Ligtenberg, S. R.
972 M., van den Broeke, M. R. and Bamber, J. L.: Dynamic thinning of glaciers on the Southern
973 Antarctic Peninsula, Science (80-.)., 348(6237), 899–903, doi:10.1126/science.aaa5727, 2015.
974 Zwally, H. J., Bindschadler, R. a, Brenner, a C., Major, J. a and Marsh, J. G.: Growth of
975 greenland ice sheet: measurement., Science, 246(4937), 1587–1589,
976 doi:10.1126/science.246.4937.1587, 1989.
977 Zwally, H. J., Giovinetto, M. B., Li, J., Cornejo, H. G. and Beckley, M. a: Mass changes of the
978 Greenland and Antarctica ice sheets and shelves and contributions to sea level rise: 1992-2002,
979 J. Glaciol., 51(175), 509, doi:10.3189/172756505781829007, 2005.
980 Zwally, H. J., Jun, L., Brenner, A. C., Beckley, M., Cornejo, H. G., Dimarzio, J., Giovinetto, M.
981 B., Neumann, T. a, Robbins, J., Saba, J. L., Donghui, Y. and Wang, W.: Greenland ice sheet
982 mass balance: distribution of increased mass loss with climate warming; 2003–07 versus 1992–
983 2002, J. Glaciol., 57(201), 88–102, doi:10.3189/002214311795306682, 2011.
984 Zwally, H. Jay, Mario B. Giovinetto, Matthew A. Beckley, and Jack L. Saba: Antarctic and
985 Greenland drainage systems, GSFC Cryospheric Sciences Laboratory, at
986 http://icesat4.gsfc.nasa.gov/cryo_data/ant_grn_drainage_systems.php, 2012

Tables:

Table 1: Accuracy (Mean), precision (SD) and the total RMS-error (RMSE) of surface elevation from CryoSat-2 observations compared to IceBridge ATM elevations. Here, the LRM mode represents the interior of the ice sheet and SIN the marginal high relief areas.

JPL	**Mean (m)**	**SD (m)**	**RMSE (m)**
LRM	0.00	0.43	0.45
SIN	-0.52	0.58	0.82
ESA	**Mean (m)**	**SD (m)**	**RMSE (m)**
LRM	-1.06	0.89	1.40
SIN	-0.90	1.05	1.13

992 *Table 2: Accuracy (Mean), precision (SD) and the total RMS-error (RMSE) of surface elevation*
993 *changes from CryoSat-2 derived from two independent methods [Surface Fit (SF) and the*
994 *Crossover (XO) method], compared to IceBridge ATM data.*

JPL - LRM	**Mean (m)**	**SD (m)**	**RMSE (m)**
SF	0.11	0.67	0.70
XO	0.24	0.72	0.78
ESA - LRM	**Mean (m)**	**SD (m)**	**RMSE (m)**
SF	0.25	1.51	1.57
XO	0.60	1.02	1.20
JPL - SIN	**Mean (m)**	**SD (m)**	**RMSE (m)**
SF	0.30	0.58	0.66
XO	-0.60	1.26	1.26
ESA - SIN	**Mean (m)**	**SD (m)**	**RMSE (m)**
SF	0.34	1.06	1.11
XO	-0.21	1.44	1.44

995
996

997 Table 3: Validation of four different DEMs, compared to IceBridge ATM elevation data. Based
998 on the weighted (number of samples) average of the four different ATM campaigns from 2011 to
999 2014. Elevation values at each ATM location were estimated by bilinear interpolation for each
1000 DEM product.

DEM	Mean (m)	SD (m)	RMSE (m)
AWI	-1.35	5.95	6.12
GIMP	-1.13	7.22	7.32
JPL	-0.87	6.31	6.39
ESA	-2.83	6.13	6.76

1001
1002

Table 4: Individual basin volume changes (km^3a^{-1}) for the Surface-Fit (SF) and Crossover (XO) method for the JPL and ESA product for the time period Jan-2011 to Jan-2015, with corresponding volumetric error.

Basin	SF – JPL	XO – JPL	SF - ESA	XO - ESA
1	-26 ± 8	-23 ± 12	-9 ± 14	-11 ± 15
2	5 ± 8	0 ± 13	31 ± 16	30 ±16
3	-38 ± 9	-34 ± 19	-46 ± 16	-31 ± 23
4	-36 ± 7	-37 ± 15	-42 ± 12	-16 ± 18
5	-19 ± 4	-27 ± 11	-19 ± 7	-6 ± 13
6	-72 ± 7	-71 ± 12	-75 ± 13	-79 ± 18
7	-56 ± 7	-51 ± 10	-41 ± 14	-35 ± 15
8	-48 ± 8	-45 ± 12	-23 ± 15	-27 ± 17
TOT	**-289 ± 20**	**-288 ± 37**	**-224± 38**	**-174 ± 48**

Figures:

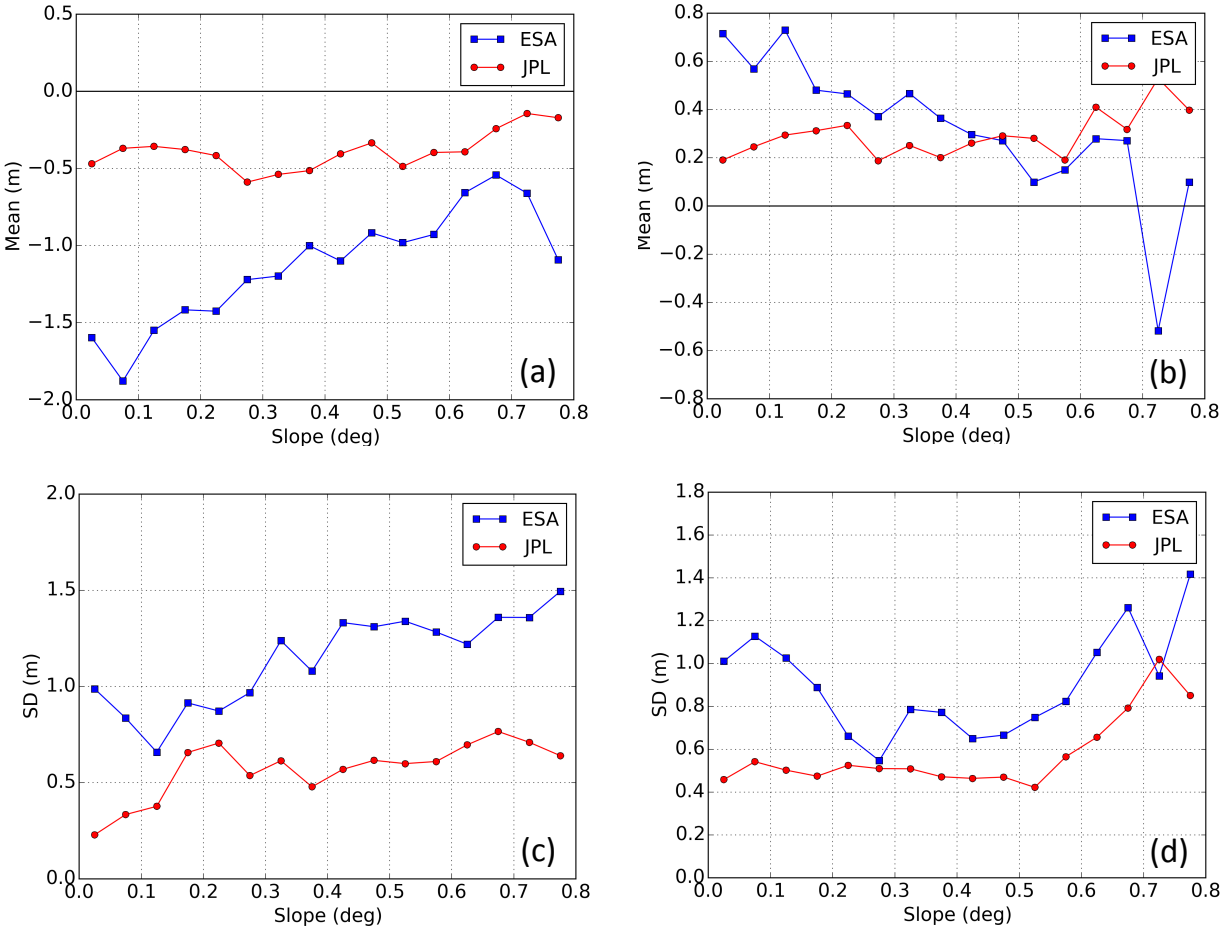

Figure 1: Validation of surface elevations (2012) (a,c) and surface elevation changes (2011-2014) (b,d) compared to IceBridge ATM, as a function of surface slope. The accuracy of the measurement is defined as the mean-value (Mean) of the CryoSat-2-ATM residuals and the precision as the standard deviation (SD).

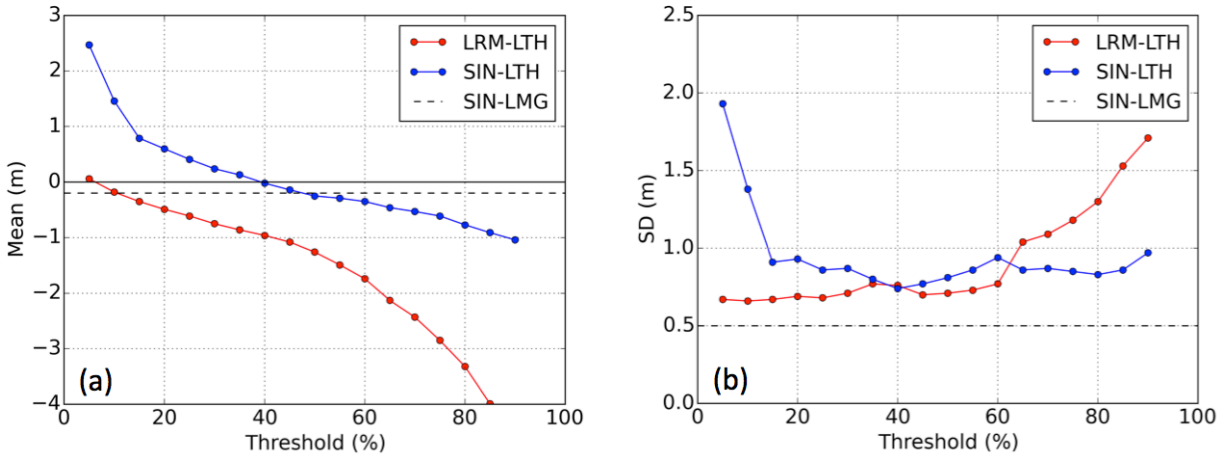

Figure 2: Comparison of accuracy (a) and precision (b) as a function of the retracking threshold for the leading edge threshold retracker (LTH, dots) applied to the of the LRM (red) and SIN (blue) data and the leading edge maximum gradient retracker (LMG, dashed grey line) applied to the SIN data over Jakobshavn Isbræ and the region around the NEEM camp (77°27'N 51°3.6'W). The accuracy (mean) and the precision (standard deviation) has for each threshold level been determined using near coincident ATM elevation, within a search radius of 50 m. The statistics was estimated using CryoSat-2 data from March-May 2013 and compared to ATM data from April 2013.

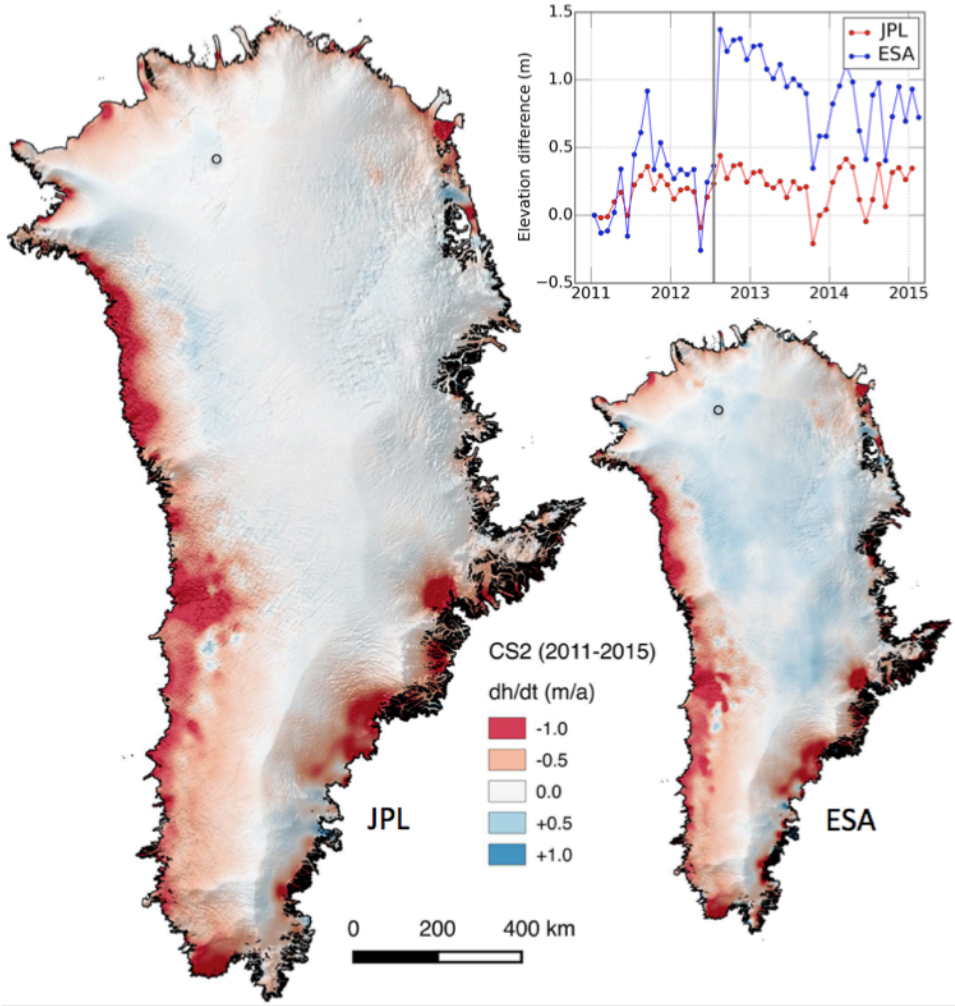

Figure 3: 2011-2015 elevation changes estimated from the surface-fit methods for the estimated L2 products. The time series depicted in the figure has been extracted at the NEEM camp (77°27'N 51°3.6'W), indicated by the black circle in both maps. The time series show the effect of the 2012 melt event, indicated by the grey vertical line, on the retrieved surface elevations. The JPL product produced a total volume change of -289 ± 20 $km^3 a^{-1}$ while the estimated total volume change of the ESA product was -224 ± 38 $km^3 a^{-1}$. This corresponds to -29 versus 38 $km^3 a^{-1}$ (H > 2000 m) and -259 versus -262 $km^3 a^{-1}$ (H < 2000 m) for the JPL and ESA product respectively. Images have been smoothed with a 10 km median filter for visualization purposes. The 1x1 km ice sheets mask used in this figure was constructed from polygons obtained from Frank Paul at the University of Zurich (personal communication).

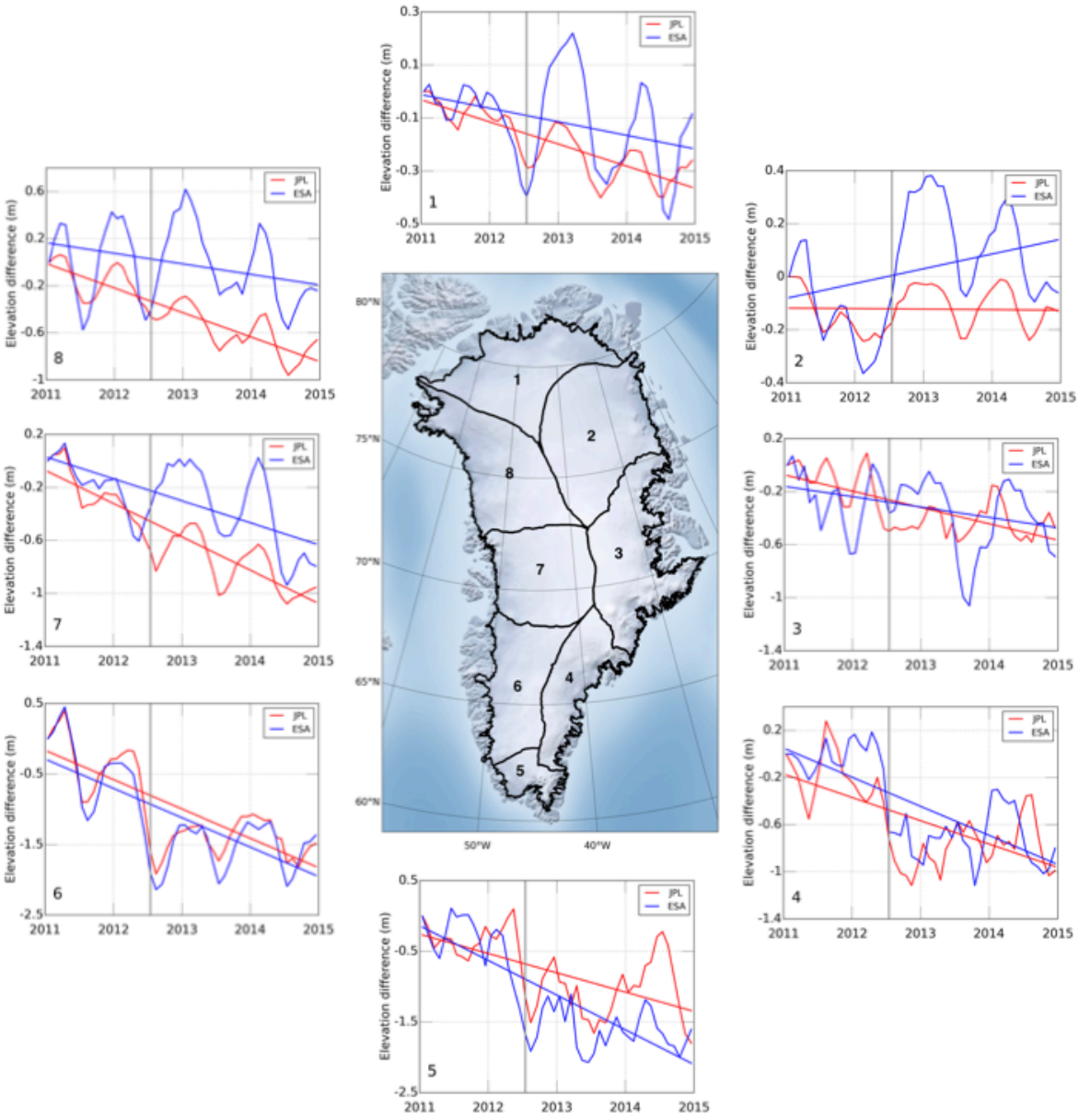

Figure 4. Monthly elevation change time-series for 8 large drainage basins of the Greenland Ice Sheet generated from the ESA (red) and the JPL solution (blue). Time-series have been smoothed using a 3-month moving average for improved visualization. The grey vertical line indicates the timing of the 2012 melt event.

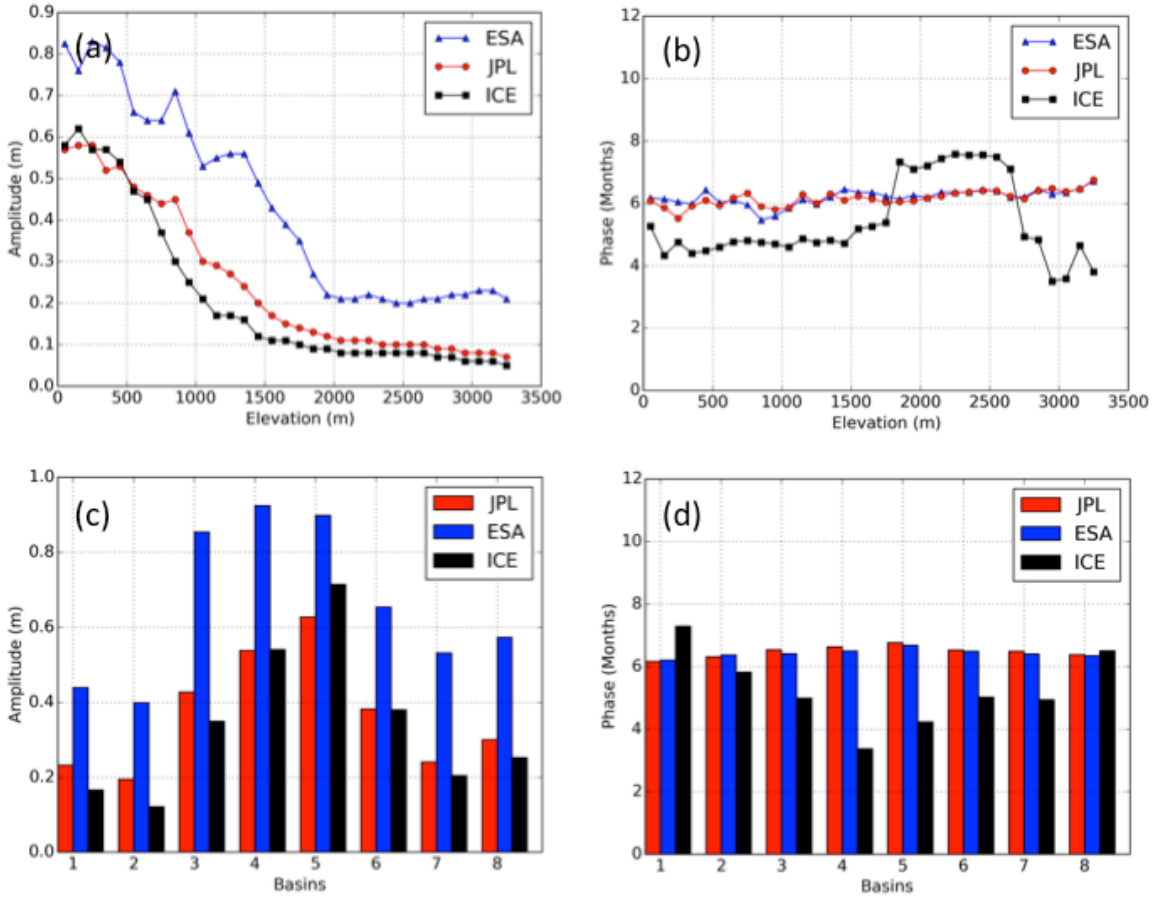

Figure 5: Estimated seasonal amplitude (a,c) and phase of the maximum amplitude (b,d) from the surface-fit method for CryoSat-2 [ESA (blue) and JPL (red)] compared to ICESat (ICE, black)). Values are compared using a search radius of 50 m, using the closest point within this distance, and the phase offset is referenced from 1st of January. The values of amplitude and phase are then binned according to elevation using the median value within 100 m intervals

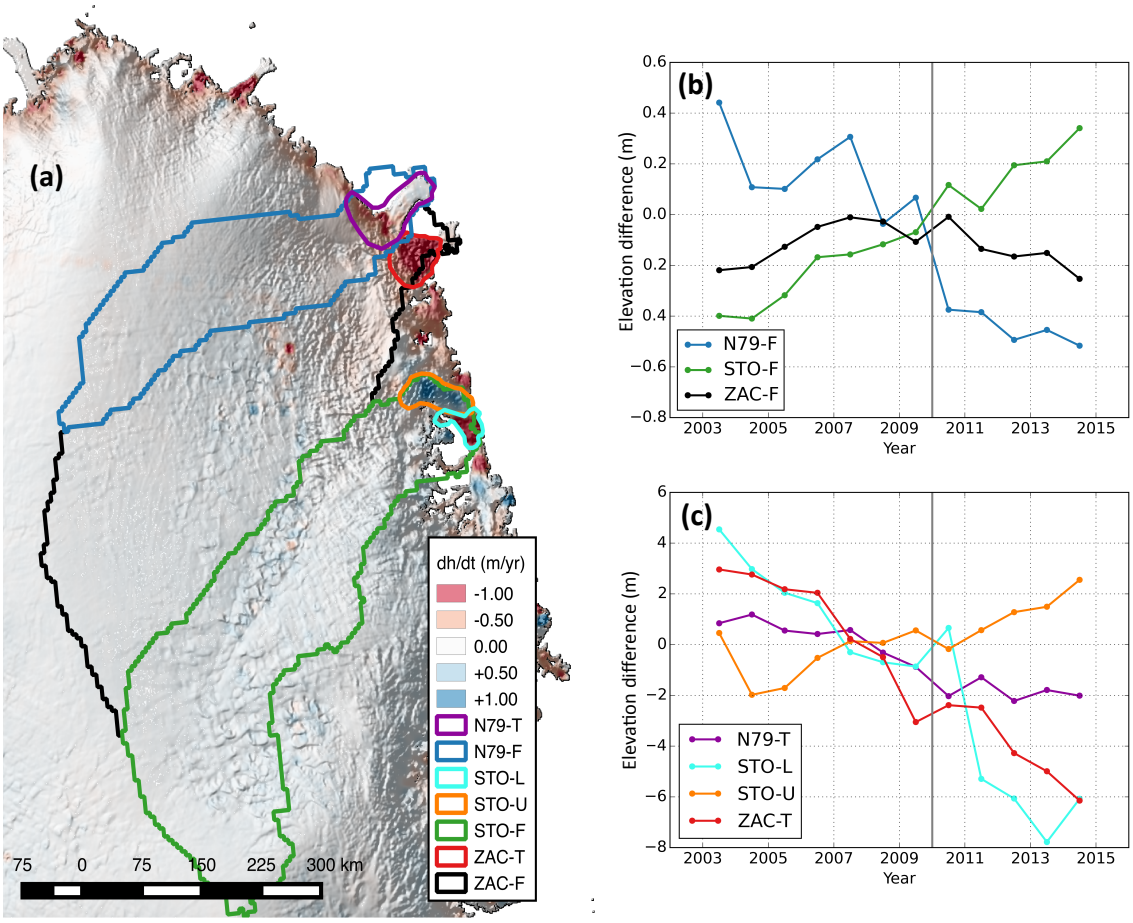

Figure 6: Northeast part of the Greenland Ice Sheet showing surface elevation change (a) from CryoSat-2 JPL-solution (2011-2015), with corresponding hydrological basin outlines. The hydrological basins are separated into full basins size (b) and to the terminus areas (c). Sub-figures (b) and (c) shows a merged 12 year annual elevation time series from ICESat and CryoSat-2 for each color-coded area in (a). The derived elevation time series was formed using the surface-fit method described in Section (3.1) onto a 500 m grid to facilitate merging of the two data sets due to their difference in orbit characteristics. The elevation change map is overlaid onto the CryoSat-2 hill shaded DEM based on surface heights from Jul-2010 to Feb-2015. The annual 12-year time series was created from the surface-fit method by binning the monthly values into annual values using the median of the corresponding 12 months.